

See discussions, stats, and author profiles for this publication at: <https://www.researchgate.net/publication/265094630>

# Free-Standing Hierarchically Sandwich-Type Tungsten Disulfide Nanotubes/Graphene Anode for Lithium-Ion Batteries

ARTICLE *in* NANO LETTERS · AUGUST 2014

Impact Factor: 13.59 · DOI: 10.1021/nl502848z · Source: PubMed

---

CITATIONS

23

---

READS

85

13 AUTHORS, INCLUDING:



**Weiping Wu**

University of Cambridge

154 PUBLICATIONS 4,518 CITATIONS

SEE PROFILE



**Li Li**

Beijing Institute of Technology

88 PUBLICATIONS 1,386 CITATIONS

SEE PROFILE



**Deia Abd El-Hady**

Assiut University

56 PUBLICATIONS 501 CITATIONS

SEE PROFILE

# Free-Standing Hierarchically Sandwich-Type Tungsten Disulfide Nanotubes/Graphene Anode for Lithium-Ion Batteries

Renjie Chen,<sup>\*,†,⊥</sup> Teng Zhao,<sup>†,⊥</sup> Weiping Wu,<sup>‡</sup> Feng Wu,<sup>\*,†</sup> Li Li,<sup>†</sup> Ji Qian,<sup>†</sup> Rui Xu,<sup>§</sup> Huiming Wu,<sup>§</sup> Hassan M. Albishri,<sup>||</sup> A. S. Al-Bogami,<sup>||</sup> Deia Abd El-Hady,<sup>||</sup> Jun Lu,<sup>\*,§</sup> and Khalil Amine<sup>\*,§,||</sup>

<sup>†</sup>Beijing Key Laboratory of Environmental Science and Engineering, School of Chemical Engineering and Environment, Beijing Institute of Technology, Beijing 100081, China

<sup>‡</sup>Cambridge Ink Technology Ltd., 91 Devonshire Mews, Devonshire Road, Cambridge CB1 2BB, United Kingdom

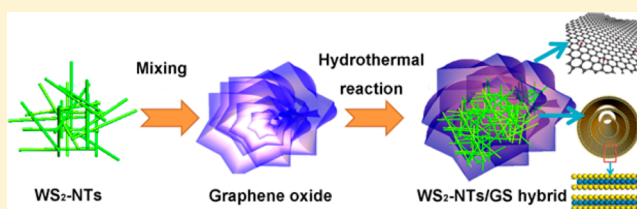
<sup>§</sup>Chemical Sciences and Engineering Division, Argonne National Laboratory, 9700 South Cass Avenue, Lemont Illinois 60440, United States

<sup>||</sup>Faculty of Science, King Abdulaziz University, 80203 Jeddah, Saudi Arabia

## S Supporting Information

**ABSTRACT:** Transition metal dichalcogenides (TMD), analogue of graphene, could form various dimensionalities. Similar to carbon, one-dimensional (1D) nanotube of TMD materials has wide application in hydrogen storage, Li-ion batteries, and supercapacitors due to their unique structure and properties. Here we demonstrate the feasibility of tungsten disulfide nanotubes (WS<sub>2</sub>-NTs)/graphene (GS) sandwich-type architecture as anode for lithium-ion batteries for the first time. The graphene-based hierarchical architecture plays vital roles in achieving fast electron/ion transfer, thus leading to good electrochemical performance. When evaluated as anode, WS<sub>2</sub>-NTs/GS hybrid could maintain a capacity of 318.6 mA/g over 500 cycles at a current density of 1A/g. Besides, the hybrid anode does not require any additional polymeric binder, conductive additives, or a separate metal current-collector. The relatively high density of this hybrid is beneficial for high capacity per unit volume. Those characteristics make it a potential anode material for light and high-performance lithium-ion batteries.

**KEYWORDS:** Lithium-ion batteries, anode material, graphene, tungsten disulfide nanotube, sandwich-type structure, electrochemical performance



Rechargeable lithium ion batteries (LIBs) have long been considered as the most effective energy-storage technology and dominated portable electronic market for over two decades.<sup>1,2</sup> On the basis of the intercalation mechanism, state-of-the-art Li-ion technology can exhibit a theoretical specific energy of ~400 Wh/kg, such as LiCoO<sub>2</sub>/graphite system.<sup>3</sup> However, it is urgent to explore new chemistries and materials that can significantly increase the cell energy density, considering the future demand for electronic vehicles and large-scale energy storage plants.<sup>4,5</sup>

Graphite, a widely used anode material for the current LIBs, has a theoretical capacity of only 372 mAh/g, given a fully intercalated LiC<sub>6</sub> compound, which is one of the limiting factors for achieving high energy density of the cell.<sup>6</sup> In order to overcome such technical bottleneck, considerable effort has been devoted to design and synthesize new anode materials with higher theoretical specific capacity, such as transition metal oxides (SnO<sub>2</sub>, Co<sub>3</sub>O<sub>4</sub>, Fe<sub>3</sub>O<sub>4</sub>), Sn, and Si.<sup>7</sup> However, all these materials suffer from severe volume variation during charge–discharge cycling, which results in serious pulverisation of the electrodes and thus rapid capacity degradation. For instance, Si has a high specific capacity of 4200 mAh/g if fully lithiated to Li<sub>4.4</sub>Si, however, it also shows a large volume expansion up to

400%. Such volume expansion causes huge mechanical stress of the electrode and therefore severely limits the lifetime of Si anode. Although various strategies have been proposed to enhance the structural stability of Si-based materials, including carbon or polymer coating,<sup>8,9</sup> nanostructuring,<sup>10–12</sup> and hierarchical hybridization,<sup>13–15</sup> it is still very challenge to overcome the issue of the inherent volume change of these materials during cycling.

Transition metal dichalcogenides (TMD) MX<sub>2</sub> (M = Mo, Ti, V, and W, X = S or Se)<sup>16,17</sup> with the similar feature of layered structure as graphite could have great potential for alternative anode materials. In general, MX<sub>2</sub> has strong covalent bonds within layers and weak van der Waals forces between layers, which provide ideal space for intercalation of lithium ions. For instance, MoS<sub>2</sub> has much larger spacing between neighboring layers (0.615 nm) than that of graphite (0.335 nm) and weak van der Waals forces between the layers, which in principal may make the Li<sup>+</sup> diffuse easier. However, certain electrochemical properties of MX<sub>2</sub> can only be achieved in their 1D or 2D

**Received:** July 24, 2014

**Revised:** August 21, 2014

**Published:** August 27, 2014

nanostructured crystals because of the relatively high resistance for Li-ion transport in their bulk form. In addition, the electron conductivity of this type of material is still too low, which could lead to rapid capacity fading and poor rate performance when using as the anode material in a Li-ion cell. A widely used approach to overcome this problem is to design and optimize nanocomposites for good electrical conductivity, because nanostructured TMD likely allows to increase Li-ion intercalation/deintercalation due to the high surface area and shorter diffusion path for Li-ion transport.

Among these TMD compounds,  $\text{MoS}_2$ , as the most studied TMD for  $\text{Li}^+$  storage today, has received considerable attention as a possible anode candidate for Li-ion cells. For instance,  $\text{MoS}_2$ -C nanotube<sup>18</sup> and graphene/ $\text{MoS}_2$  nanoflake<sup>19</sup> have been reported with significant improvement in cycle life and rate performance by taking advantages of the large electrolyte-electrode interface and reduced ion diffuse pathway. On the other hand,  $\text{WS}_2$  with higher intrinsic electrical conductivity than  $\text{MoS}_2$ ,<sup>20</sup> which is not studied in detail yet, could be a more suitable candidate as the anode material for Li-ion cells.

Herein, we propose a conceptually new approach to design and fabricate a novel three-dimensional  $\text{WS}_2$  nanotubes/graphene ( $\text{WS}_2$ -NTs/GS) hybrid with unique sandwich-type architecture via a simple one-pot hydrothermal reaction. As shown in Figure 1,  $\text{WS}_2$ -NTs/GS hybrid was easily prepared by

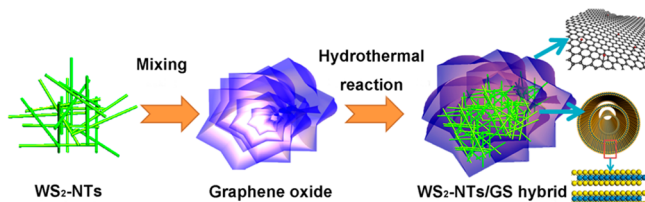


**Figure 1.** Schematic illustration of the fabrication of 3D hierarchically structured  $\text{WS}_2$ -NTs/GS hybrid.

dispersion of  $\text{WS}_2$ -NTs into homogeneous graphene oxide (GO) solution and subsequent hydrothermal reaction at controlled pH value for conversion of GO to GS.<sup>21</sup> GS could curl and cross-link to form 3D network during dehydration due to the combination of hydrophobic nature and  $\pi$ - $\pi$  interactions<sup>22</sup> while  $\text{WS}_2$ -NT was embedded into the galleries of GS. More importantly, controlling pH of solution by adding appropriate amount of ammonia could further enhance those assemble in a compact manner.<sup>23</sup> The procedure is detailed in the experimental section of the Supporting Information. The unique hybrid could benefit from the synergistic effects of its each component. Specifically, the imbedded  $\text{WS}_2$ -NTs could effectively prevent GS from complete restacking, thus affording pores and channel for ion diffusion. Meanwhile, the good electrical and mechanical properties of GS could not only enhance the anode conductivity but also accommodate the volume change of anode during cycling. As a result,  $\text{WS}_2$ -NTs/GS hybrid exhibited improved cycling stability and rate capability compared with that of  $\text{WS}_2$ -NTs.

X-ray diffraction (XRD) patterns of  $\text{WS}_2$ -NTs and  $\text{WS}_2$ -NTs/GS are shown in Figure 2A. The analysis of  $\text{WS}_2$ -NTs hybrid spectrum shows highly crystalline hexagonal structure (JCPDS No. 84-1398). For  $\text{WS}_2$ -NTs/GS hybrid, all the diffraction peaks are consistent with that of  $\text{WS}_2$ -NTs except for an additional small and broad peak appearing at  $2\theta$  of  $24$ – $26^\circ$  (inset). Such peak originates from the (002) plane of GS,

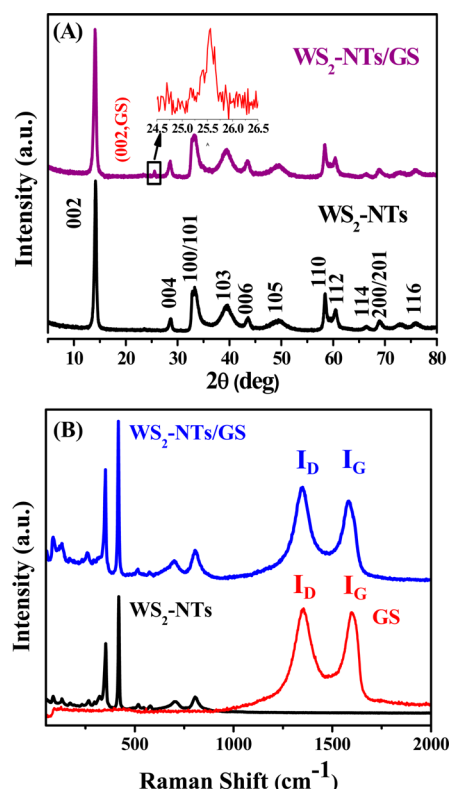


**Figure 2.** (A) XRD patterns of  $\text{WS}_2$ -NTs and  $\text{WS}_2$ -NTs/GS hybrid; (B) Raman spectra of  $\text{WS}_2$ -NTs/GS hybrid with those of  $\text{WS}_2$ -NT and GS.

indicating a disordered stack of graphene sheet. These results suggest that the attachment of  $\text{WS}_2$ -NTs on GS does not influence its crystallinity and no new phases are generated.

To further elucidate the effect of the deposition of  $\text{WS}_2$ -NTs on the microstructure of graphene, Raman spectroscopy was carried out to characterize the carbon lattice in the  $\text{WS}_2$ -NTs/GS hybrid (Figure 2B). The Raman spectrum of pure graphene (GS) showed a pattern of partially graphitized carbon. The peak at  $\sim 1350\text{ cm}^{-1}$  (D band) is assigned to defects and disorder in the graphene layer while peaks at  $\sim 1593\text{ cm}^{-1}$  (G band) is related to the coplanar vibration of  $\text{sp}^2$ -bonded carbon atoms in GS. Interestingly, the intensity of the D band in the  $\text{WS}_2$ -NTs/GS hybrid is higher than that of the pure GS, indicating a more disordered stack of graphene layer in the hybrid. To some extents, it reveals that the  $\text{WS}_2$ -NTs were embedded into the interlayer galleries of GS and prevented it from restacking. It should also be noted that the characteristic Raman scattering peaks for  $\text{WS}_2$ -NTs are mainly observed below  $1000\text{ cm}^{-1}$ , which is consistent with the crystalline nature of  $\text{WS}_2$ -NTs in the hybrid.<sup>24</sup>

To determine the chemical composition of  $\text{WS}_2$ -NTs/GS hybrid, X-ray photoelectron spectroscopy (XPS) analyses were conducted. According to the broad XPS scan spectrum in the region of  $0$ – $1100\text{ eV}$  (Figure 3A), four elements including W, S, C, O are detected and their atomic concentration is 7.55% W, 13.54% S, 66.91% C, and 12.00% O, respectively. The calculated atomic ratio of S to W is  $\sim 1.8$ , closed to the theoretically predicted value for  $\text{WS}_2$ . The  $\text{W}_{4f}$  XPS spectra of the hybrid exhibits peaks observed at 33.5 and 31.3 eV, corresponding to the  $\text{W}_{4f5/2}$  and  $\text{W}_{4f7/2}$  characteristic peaks of  $\text{WS}_2$ -NTs (Figure 3B). As for the peak at 36.9 eV, we assign it to the W–O bond, indicating a low surface oxidation.<sup>25</sup> The

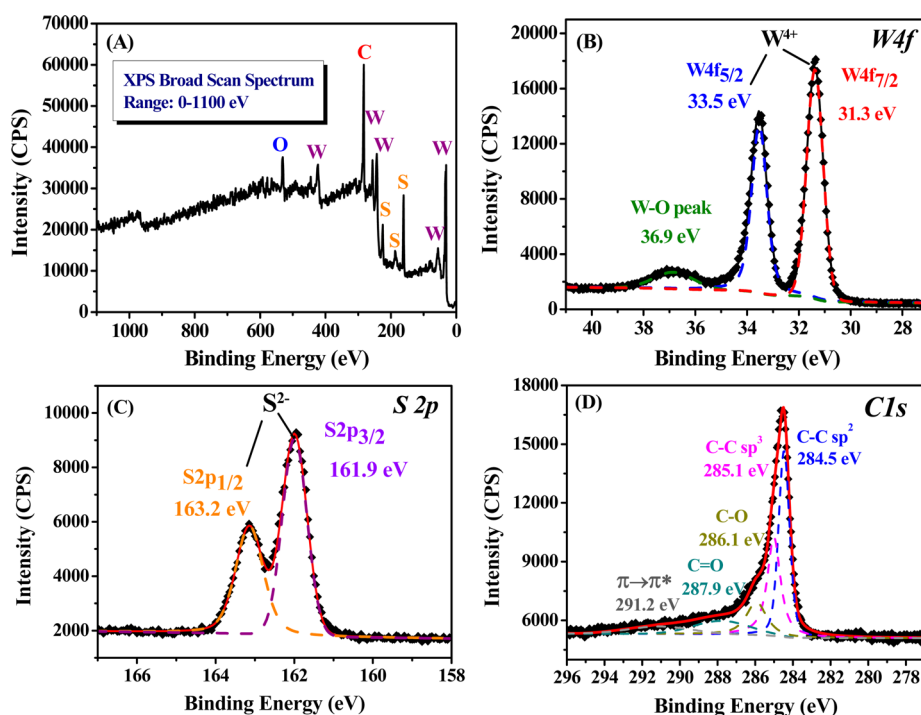


**Figure 3.** XPS spectra of WS<sub>2</sub>-NTs/GS hybrid: (A) broad scan spectrum; (B) W 4f; (C) S 2p; (D) C 1s.

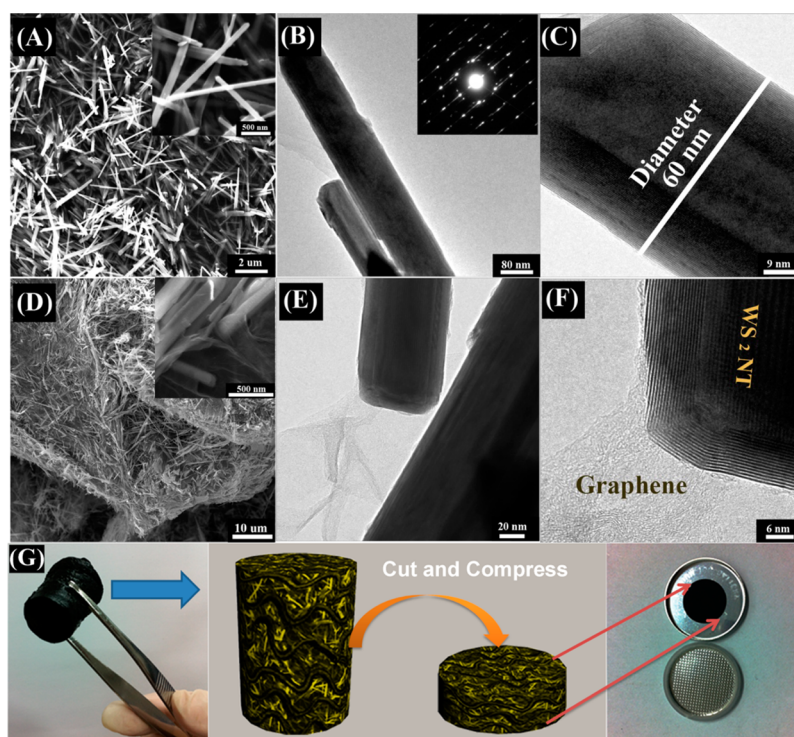


**Figure 4.** (A,D) SEM images of WS<sub>2</sub>-NTs and WS<sub>2</sub>-NTs/GS hybrid; (B,C) HR-TEM images of WS<sub>2</sub>-NTs; (E,F) HR-TEM images of WS<sub>2</sub>-NTs/GS hybrid; (G) photograph of WS<sub>2</sub>-NTs/GS hybrid and schematic illustration of the fabrication of WS<sub>2</sub>-NTs/GS anode in standard CR 2025 coin cell.

presence of WS<sub>2</sub>-NTs can be further confirmed by the two distinct S<sub>2p</sub> peaks at 161.9 and 163.2 eV, which correspond to the S<sub>2p3/2</sub> and S<sub>2p1/2</sub> components of WS<sub>2</sub>-NTs (Figure 3C). Besides, C 1s (284.5 eV) and O 1s (530 eV) peaks are mainly attributed to the carbon and oxygen atom in GS. The deconvolution of the C 1s peaks is displayed in Figure 3D. Peaks centered at 286.1 and 287.9 eV are attributed to the

residual C—O and C=O groups, respectively. Compared with the case of GO,<sup>26</sup> the peak intensities of most oxygen containing groups decrease remarkably, indicating the restoration of sp<sup>2</sup> hybridized carbon network. Meanwhile, the O/C ratio was 1:5.6 for the hybrid, which was also consistent with the reduction degree of GO by dehydration mechanism.<sup>27</sup> Accordingly, we can conclude that the hybrid consists of GS



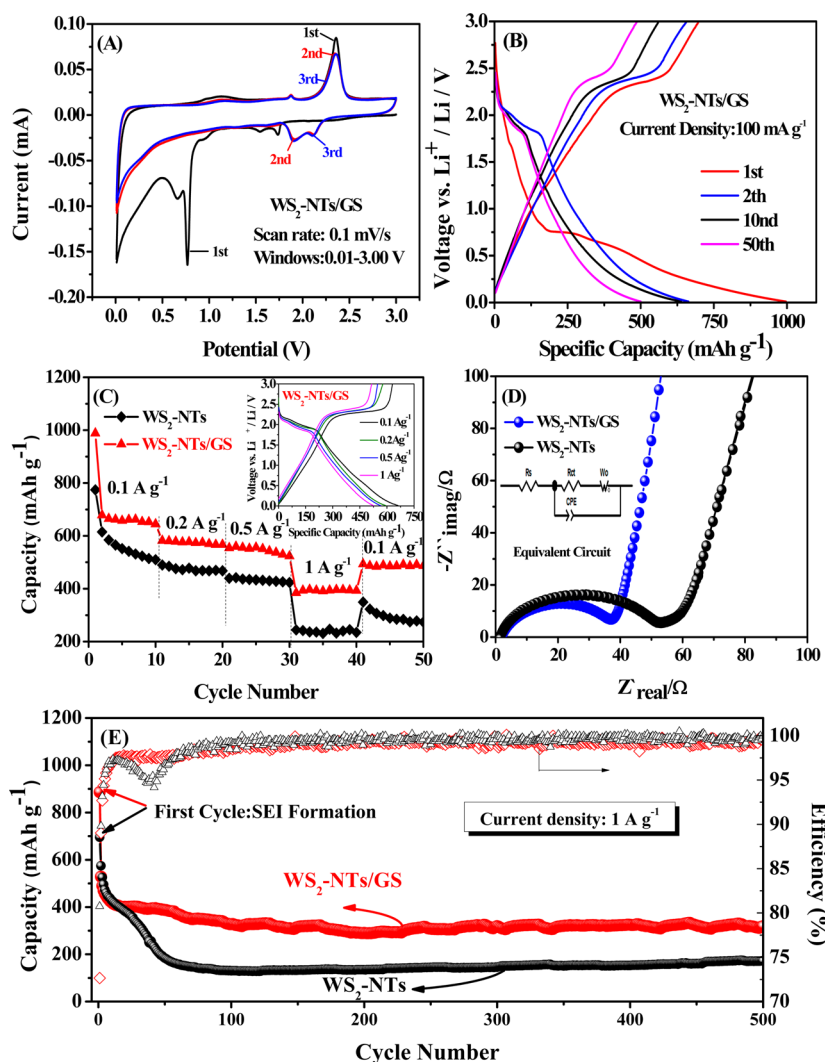


**Figure 5.** (A) Cyclic voltammetry of the WS<sub>2</sub>-NTs/GS hybrid anode over a voltage range of 0.01–3.00 V at a scanning rate of 0.1 mV/s. (B) Discharge/charge voltage profiles of WS<sub>2</sub>-NTs/GS hybrid anode at a current density of 100 mA/g. (C) Rate capabilities of WS<sub>2</sub>-NTs/GS hybrid and WS<sub>2</sub>-NTs anode; inset: discharge/charge voltage profiles of WS<sub>2</sub>-NTs/GS hybrid at current density of 0.1, 0.2, 0.5, and 1 A/g. (D) Nyquist plots of the WS<sub>2</sub>-NTs/GS hybrid and WS<sub>2</sub>-NTs anode at open potential before cycling. (E) Cycling stability of WS<sub>2</sub>-NTs/GS hybrid and WS<sub>2</sub>-NTs anode at 1 A/g for 500 cycles.

and WS<sub>2</sub>-NTs, whose content are about 35.4 and 64.6 wt %, respectively.

The morphology and structure of the WS<sub>2</sub>-NTs/GS hybrid were characterized by scanning electron microscopy (SEM) and transmission electron microscopy (TEM). The SEM image (Figure 4A) of WS<sub>2</sub>-NTs exhibits a uniform one-dimensional (1D) structure with diameter of around 60 nm and length of about 5 μm. Like carbon nanotubes, such straight structure could easily form bundles, which provide extra lithium intercalation between intertubular sites. Figure 4B shows the electron diffraction pattern of two parallel WS<sub>2</sub>-NTs. The {10 $\bar{1}$ 0} spots appear to be arranged in a double-hexagonal pattern, corresponding to in plane diffractions in each tube.<sup>28</sup> The HR-TEM image (Figure 4C) of individual WS<sub>2</sub>-NTs clearly displays the hollow interior and multiwalls. Compared with straight WS<sub>2</sub>-NTs, WS<sub>2</sub>-NTs/GS hybrid display a three-dimensional (3D) sandwich-like architecture that individual WS<sub>2</sub> nanotubes are homogeneously incorporated into the interlayer galleries of graphene sheets (Figure 4D). From the magnified SEM (inset), we can see that thin graphene could

easily wrap around WS<sub>2</sub>-NTs due to its flexibility. The microstructure of WS<sub>2</sub>-NTs/GS hybrid was further analyzed by HR-TEM (Figure 4D,E). It is clear that WS<sub>2</sub>-NTs bundles were well dispersed in graphene matrices. According to the cross-sectional images, there are about five layer graphene sheets wrapping around the edges of WS<sub>2</sub>-NTs, which have a *d*-spacing of approximately 0.62 nm twice than that of GS (~0.34 nm). Figure 4G shows the photograph of the black cylinder of the assembled WS<sub>2</sub>-NTs/GS hybrid, which can be cut and compressed into circular pellet with a diameter of 11 mm for direct use as anode in standard CR 2025 coin cell.

To investigate the anode performance of the WS<sub>2</sub>-NTs/GS hybrid, electrochemical characterization was conducted based on two-electrode coin-type cells (CR 2025) with Li metal as the counter-electrode. Figure 5A shows cyclic voltammograms (CV) of the WS<sub>2</sub>-NTs/GS hybrid anode for the initial three cycles between 0.01 and 3.00 V at a scan rate of 0.1 mV/s. In the first cycles, two small cathodic peaks at 1.6 and 1.5 V are observed, which correspond to the lithium insertion to WS<sub>2</sub> to form Li<sub>x</sub>WS<sub>2</sub>. The following sharp overlap peak at 0.75 V could

be attributed to the subsequent conversion reaction of Li with  $\text{WS}_2$  and the formation of a solid electrolyte interlayer (SEI).<sup>29,30</sup> The starting cathodic peak at 0.5 V is related to the insertion of  $\text{Li}^+$  into graphene, which is also electroactive for lithium storage.<sup>31</sup> During the anodic scan, three oxidation peaks at 1.0, 1.6, and 2.2 V are observed, corresponding to the reverse extraction of  $\text{Li}^+$  from graphene and  $\text{Li}_x\text{WS}_2$  host, respectively. From the second cycle onward, the cathodic peak at 0.75 V disappears while the original cathodic peaks at 1.6 and 1.5 V shift to 2.1 and 1.8 V, indicating improved reversibility of lithiation and delithiation with cycling. In addition, no obvious changes are observed for the redox peaks, implying that the anode exhibits good electrochemical stability. For comparison, the CV of just  $\text{WS}_2$ -NTs is shown in Supporting Information Figure S1. It can be seen that the electrochemical behavior of  $\text{WS}_2$ -NTs is almost the same with that of  $\text{WS}_2$ -NTs/GS hybrid except the absence of redox related to the insertion/extraction of  $\text{Li}^+$  into/from GS.

Figure 5B shows the galvanostatic charge/discharge profiles of the  $\text{WS}_2$ -NTs/GS hybrid anode in the first, second, 10th and 50th at a current density of 0.1 A/g. The hybrid anode delivers an initial capacity of 996.4 mAh/g and a corresponding charge capacity of 697.7 mAh/g with a first-cycle Coulombic efficiency of  $\sim 70.0\%$ . The large discharge capacity is attributed to the formation of SEI layer and the irreversible conversion reaction between Li and  $\text{WS}_2$ , which are consistent with the above CV analysis. After the initial capacity loss, a high capacity retention upon cycling are observed and the pattern of discharge and charge plateaus remains unchanged. A capacity of 500.2 mAh/g is achieved after 50 cycles. For comparison, pure  $\text{WS}_2$ -NTs were tested under the same current density as that for the  $\text{WS}_2$ -NTs/GS hybrid anode (Supporting Information Figure S2). The first discharge and charge capacities for  $\text{WS}_2$ -NTs anode are 768.5 and 660.8 mAh/g, respectively. Also, serious capacity decay is observed with cycling, accompanied by the gradual disappearance of discharge plateaus at  $\sim 2.0$  V. After 50 cycles, the capacity of  $\text{WS}_2$ -NTs anode dramatically decreases to 202.8 mAh/g.

Figure 5C reveals tenth-cycle discharge capacities of around 692.6, 574.8, 546.2, and 393.5 mAh/g at current density of 0.1, 0.2, 0.5, and 1.0 A/g, respectively. Besides, the specific capacity of  $\text{WS}_2$ -NTs/GS hybrid anode could recover to 487.9 mAh/g when the current density is returned to 0.1 A/g. More importantly, the galvanostatic measurements for the  $\text{WS}_2$ -NTs/GS hybrid anode at increasing rate (inset) show the same pattern of discharge and charge plateaus, indicating good rate performance and rate tolerance. In contrast, pure  $\text{WS}_2$ -NTs anode exhibits poor capacities and rate capabilities. Even when the current density reduced, the capacity cannot recover its initial level. This difference supports that the 3D hierarchical structure could successfully enhance electronic/ionic transport within the anode, resulting improved electrochemical kinetics, which is further evidenced by the results of EIS (Figure 5D) that the charge-transfer resistance values of  $\text{WS}_2$ -NTs/GS hybrid anode is found to be 37.5  $\Omega$ , which is lower than that of  $\text{WS}_2$ -NTs (52.6  $\Omega$ ).

Figure 5E compares the long cycle performance of  $\text{WS}_2$ -NTs and  $\text{WS}_2$ -NTs/GS hybrid anode at high current density of 1 A/g. In the case of  $\text{WS}_2$ -NTs/GS hybrid anode, the initial capacity is as high as 886.1 mAh/g and it still maintains a capacity of 318.6 mAh/g after 500 cycles. In contrast, much more capacity decay is observed for  $\text{WS}_2$ -NTs. The specific capacity dramatically decreases from 695.4 mAh/g to 171.9 mAh/g

after 500 cycles. The good cycle performance of  $\text{WS}_2$ -NTs/GS hybrid anode benefits from the following factors: (1) the incorporation of GS significantly enhances the conductivity of anode; (2) the hybrid 3D architecture consisting of layered  $\text{WS}_2$ -NTs and GS affords pores and large electrolyte/electrode interface, thus providing channels for Li-ion diffusion and reactive sites for Li-ion intercalation; and (3) the flexible GS could effectively accommodate the volume change during cycling.

In summary, we have demonstrated the feasibility of  $\text{WS}_2$  nanotube/graphene sandwich-type architecture for good electrochemical performance. To the best of our knowledge, it is the first time for reporting such a conceptual design. Compared with pure  $\text{WS}_2$ -NTs, the hybrid anode exhibits much improved cycling stability and rate capability without additional polymeric binder, conductive additives, or a separate metal current-collector. More importantly, the relatively high density of this hybrid is beneficial for high capacity per unit volume, which offsets its poor operating potential and thus makes it a promising anode material for light and high performance lithium-ion batteries.

## ■ ASSOCIATED CONTENT

### Supporting Information

Detail of experimental and additional figures depicting experiment results. This material is available free of charge via the Internet at <http://pubs.acs.org>.

## ■ AUTHOR INFORMATION

### Corresponding Authors

\*E-mail: (R.C.) [chenrj@bit.edu.cn](mailto:chenrj@bit.edu.cn).

\*E-mail: (F.W.) [wufeng863@vip.sina.com](mailto:wufeng863@vip.sina.com).

\*E-mail: (J.L.) [junlu@anl.gov](mailto:junlu@anl.gov).

\*E-mail: (K.A.) [amine@anl.gov](mailto:amine@anl.gov).

### Author Contributions

<sup>†</sup>R.C. and T.Z. contributed equally to this work.

### Notes

The authors declare no competing financial interest.

## ■ ACKNOWLEDGMENTS

This work was supported by the National Science Foundation of China (NSFC, 21373028), the National 863 Program (2011AA11A256), New Century Educational Talents Plan of Chinese Education Ministry (NCET-12-0050), and Beijing Nova Program (Z121103002512029). This work was also supported by the U.S. Department of Energy under Contract DE-AC0206CH11357 from the Vehicle Technologies Office, Department of Energy, Office of Energy Efficiency and Renewable Energy (EERE) and Division of Materials Science, Basic Energy Sciences, Department of Energy, Office of Science. Argonne National Laboratory, a U.S. Department of Energy Office of Science laboratory, is operated under Contract No. DE-AC02-06CH11357. This project was also funded by the Deanship of Scientific research (DSR), King Abdulaziz University, Jeddah under the HiCi Project (Grant 11-130-1434HiCi). The authors (H.M.A., D.A.E., A.S.A., and K.A.) thank the DSR for their technical and financial support. The authors also acknowledge the U.S.–China Electric Vehicle and Battery Technology Collaboration between Argonne National Laboratory and Beijing Institute of Technology.

## ■ REFERENCES

- (1) Armand, M.; Tarascon, J. M. *Nature* **2008**, *451*, 652–657.
- (2) Scrosati, B.; Garche, J. *J. Power Sources* **2010**, *195*, 2419–2430.
- (3) Kang, B.; Ceder, G. *Nature* **2009**, *458*, 190–193.
- (4) Tarascon, J. M.; Armand, M. *Nature* **2001**, *414*, 359–367.
- (5) Dunn, B.; Kamath, H.; Tarascon, J.-M. *Science* **2011**, *334*, 928–935.
- (6) Wu, Y. P.; Rahm, E.; Holze, R. *J. Power Sources* **2003**, *114*, 228–236.
- (7) Tirado, J. L. *Mater. Sci. Eng. R* **2003**, *40*, 103–136.
- (8) Wang, C.; Wu, H.; Chen, Z.; McDowell, M. T.; Cui, Y.; Bao, Z. *Nat. Chem.* **2013**, *5*, 1042–1048.
- (9) Chen, Z.; Zhou, M.; Cao, Y.; Ai, X.; Yang, H.; Liu, J. *Adv. Energy Mater.* **2012**, *2*, 95–102.
- (10) Bruce, P. G.; Scrosati, B.; Tarascon, J.-M. *Angew. Chem., Int. Ed.* **2008**, *47*, 2930–2946.
- (11) Chan, C. K.; Peng, H.; Liu, G.; McIlwrath, K.; Zhang, X. F.; Huggins, R. A.; Cui, Y. *Nat. Nanotechnol.* **2008**, *3*, 31–35.
- (12) Arico, A. S.; Bruce, P.; Scrosati, B.; Tarascon, J.-M.; van Schalkwijk, W. *Nat. Mater.* **2005**, *4*, 366–377.
- (13) Magasinski, A.; Dixon, P.; Hertzberg, B.; Kvit, A.; Ayala, J.; Yushin, G. *Nat. Mater.* **2010**, *9*, 353–358.
- (14) Zhou, G.; Wang, D.-W.; Li, F.; Zhang, L.; Li, N.; Wu, Z.-S.; Wen, L.; Lu, G. Q.; Cheng, H.-M. *Chem. Mater.* **2010**, *22*, 5306–5313.
- (15) Wang, H.; Cui, L.-F.; Yang, Y.; Sanchez Casalongue, H.; Robinson, J. T.; Liang, Y.; Cui, Y.; Dai, H. *J. Am. Chem. Soc.* **2010**, *132*, 13978–13980.
- (16) Ghorbani-Asl, M.; Zibouche, N.; Wahiduzzaman, M.; Oliveira, A. F.; Kuc, A.; Heine, T. *Sci. Rep.* **2013**, *3*, 2961.
- (17) Zak, A.; Feldman, Y.; Lyakhovitskaya, V.; Leitens, G.; Popovitz-Biro, R.; Wachtel, E.; Cohen, H.; Reich, S.; Tenne, R. *J. Am. Chem. Soc.* **2002**, *124*, 4747–4758.
- (18) Zhang, C.; Wang, Z.; Guo, Z.; Lou, X. W. *ACS Appl. Mater. Interfaces* **2012**, *4*, 3765–3768.
- (19) Yu, H.; Ma, C.; Ge, B.; Chen, Y.; Xu, Z.; Zhu, C.; Li, C.; Ouyang, Q.; Gao, P.; Li, J.; Sun, C.; Qi, L.; Wang, Y.; Li, F. *Chem.—Eur. J.* **2013**, *19*, 5818–5823.
- (20) Zhang, C.; Ning, Z.; Liu, Y.; Xu, T.; Guo, Y.; Zak, A.; Zhang, Z.; Wang, S.; Tenne, R.; Chen, Q. *Appl. Phys. Lett.* **2012**, *101*, 113112.
- (21) Xu, Y.; Sheng, K.; Li, C.; Shi, G. *ACS Nano* **2010**, *4*, 4324–4330.
- (22) Zhou, G.; Yin, L. C.; Wang, D. W.; Li, L.; Pei, S.; Gentle, I. R.; Li, F.; Cheng, H. M. *ACS Nano* **2013**, *7*, 5367–5375.
- (23) Bi, H.; Yin, K.; Xie, X.; Zhou, Y.; Wan, N.; Xu, F.; Banhart, F.; Sun, L.; Ruoff, R. S. *Adv. Mater.* **2012**, *24*, 5124–5129.
- (24) Krause, M.; Virsek, M.; Remškar, M.; Kolitsch, A.; Möller, W. *Phys. Status Solidi B* **2009**, *246*, 2786–2789.
- (25) Ratha, S.; Rout, C. S. *ACS Appl. Mater. Interfaces* **2013**, *5*, 11427–11433.
- (26) Dreyer, D. R.; Park, S.; Bielawski, C. W.; Ruoff, R. S. *Chem. Soc. Rev.* **2010**, *39*, 228–240.
- (27) Liao, K. H.; Mittal, A.; Bose, S.; Leighton, C. S.; Mkhoyan, K. A.; Macosko, C. M. *ACS Nano* **2011**, *5*, 1253–1258.
- (28) Whitby, R. L. D.; Hsu, W. K.; Fearon, P. K.; Billingham, N. C.; Maurin, I.; Kroto, H. W.; Walton, D. R. M.; Boothroyd, C. B.; Firth, S.; Clark, R. J. H.; Collison, D. *Chem. Mater.* **2002**, *14*, 2209–2217.
- (29) Liu, H.; Su, D.; Wang, G.; Qiao, S. Z. *J. Mater. Chem.* **2012**, *22*, 17437–17440.
- (30) Wang, S.; Li, G.; Du, G.; Li, L.; Jiang, X.; Feng, C.; Guo, Z.; Kim, S. *Nanoscale Res. Lett.* **2010**, *5*, 1301–1306.
- (31) Wang, G.; Shen, X.; Yao, J.; Park, J. *Carbon* **2009**, *47*, 2049–2053.

## Supporting Information

### **Free-standing hierarchically sandwich-type tungsten disulfide nanotubes/graphene anode for lithium-ion batteries**

Renjie Chen<sup>a\*||</sup>, Teng Zhao<sup>all</sup>, Weiping Wu<sup>b</sup>, Feng Wu<sup>a\*</sup>, Li Li<sup>a</sup>, Ji Qian<sup>a</sup>, Rui Xu<sup>c</sup>, Huiming Wu<sup>c</sup>, Hassan M. Albishri<sup>d</sup>, A. S. Al-Bogami<sup>d</sup>, Deia Abd El-Hady<sup>d</sup>, Jun Lu<sup>c,\*</sup>, Khalil Amine<sup>c,d,\*</sup>.

*a Beijing Key Laboratory of Environmental Science and Engineering, School of Chemical Engineering and Environment, Beijing Institute of Technology, Beijing, 100081, China.*

*b Cambridge Ink Technology Ltd., 91 Devonshire Mews, Devonshire Road, Cambridge, CB1 2BB, United Kingdom*

*c Chemical Sciences and Engineering Division, Argonne National Laboratory, 9700 South Cass Avenue, Lemont, Illinois 60440, United States*

*d King Abdulaziz University, Faculty of Science, 80203 Jeddah, Saudi Arabia*

Corresponding Author: Renjie Chen, Feng Wu, Jun Lu, Khalil Amine

\*E-mail: chenrj@bit.edu.cn; wufeng863@vip.sina.com ; junlu@anl.gov and amine@anl.gov



## EXPERIMENTAL DETAILS

*Preparation of Graphene oxide (GO).* GO was synthesized according to a modified Hummer's method.<sup>1</sup> Natural graphite powder (1 g, TianJin Fu Chen Chemical Reagents Factory, China) with an average particle size of 25  $\mu\text{m}$  was added to a solution of  $\text{H}_2\text{SO}_4$  (34 mL) and  $\text{NaNO}_3$  (0.75 g) and vigorously stirred in an ice-water bath for 20 min.  $\text{KMnO}_4$  (5 g) was gradually added, and then the mixture was reacted for 2 h at room temperature. The reaction was terminated by addition of distilled water (50 mL) and 30%  $\text{H}_2\text{O}_2$  (5 mL). The mixture was washed with 1:10  $\text{HCl}$ /water and then deionized water until the pH of the suspension was between 6 and 7. The brown graphite oxide suspension was sonicated for 6 h, and then centrifuged at 2000 rpm for 20 min to afford a supernatant that was a stable exfoliated GO solution.

*Preparation of  $\text{WS}_2$ -NTs/GS hybrid.*  $\text{WS}_2$ -NTs (1 g) was dispersed in water/ethanol (1:1, 50 mL) and then sonicated for 30 min. Exfoliated GO solution (3 mg/mL) was added to give a GO:  $\text{WS}_2$ -NTs weight ratio of 4:6. Then, certain amount of ammonia solution was gradually dropped into the above solution to get a PH of 10.1.<sup>2</sup> The mixture was ultrasonically treated for 1 h and transferred to a 100 ml stainless steel autoclave for hydrothermal reaction, which was then heated up to 180  $^\circ\text{C}$  and kept for 48 h. After cooling, the black cylinder of  $\text{WS}_2$ -NTs/GS hydrogel was taken out by tweezer and washed with water and ethanol repeatedly. The final product was collected by drying in an oven at 30 $^\circ\text{C}$  for 24 h.

*Characterization.* Raman spectroscopy was measured on a Raman spectrometer (Renishaw-1000) with an excitation laser beam wavelength of 532 nm. X-ray diffraction measurements were performed using a diffractometer (Rigaku) with a  $\text{Cu K}\alpha$  radiation source ( $\lambda=0.154$  nm). The morphology of the composites was determined by field-emission scanning electron microscopy (FEI Quanta 250, 20 kV) and high-resolution transmission electron microscopy (JEOL-2010, 200 kV). XPS measurements were collected at room temperature with PHI-1600 ESCA spectrometer and monochromatic  $\text{AlK}_\alpha$  (1486.6 eV) X-ray source.

*Electrochemical measurements.*  $\text{WS}_2$ -NTs/GS hybrid was cut and compressed into a circular pellet with a diameter of 11 mm and directly used as anode. The mass loading of a  $\text{WS}_2$ -NTs/GS hybrid was about 1.88  $\text{mg}/\text{cm}^2$ , which was determined by weight measurements with a high-precision analytical balance (XS105 Dualrange). The  $\text{WS}_2$ -NTs anode slurries were produced by mixing 80%  $\text{WS}_2$ -NTs, 10% carbon black, and 10% polyvinylidene fluoride (PVDF) binder in N-methyl-2-pyrrolidinone (NMP). The mixtures were ball milled for 4 h to form homogeneous slurries. After stirring, the slurry was coated onto Cu foil using a roll press. The coated electrodes were dried in a vacuum oven at 60  $^\circ\text{C}$  for 24 h. The electrodes were also cut into disks with a diameter of 11 mm. Two-electrode coin cells (CR2025) with Li foil as the counter electrode were

assembled in an argon-filled glovebox for electrochemical experiments. The electrolyte used was 1.0 M  $\text{LiPF}_6$  in a 1:1 v/v mixture of ethyl carbonate (EC) and diethyl carbonate (DEC) and the separator placed between the two electrode is Celgard 2325. The cells were discharged and charged from 0.01–3.00 V at different current densities (0.1–1 A/g) using an electrochemical station (LAND, Wuhan) to test their cycle life. Cyclic voltammograms were recorded on an electrochemical workstation (CHI660D, Shanghai Chenhua) between 0.01 V and 3.00 V to characterize the redox behavior and kinetic reversibility of the cells. AC impedance was also measured using the CHI660D electrochemical workstation. The AC amplitude was  $\pm 5$  mV, and the applied frequency range was from 100 kHz to 0.1 Hz.

### Supporting Data

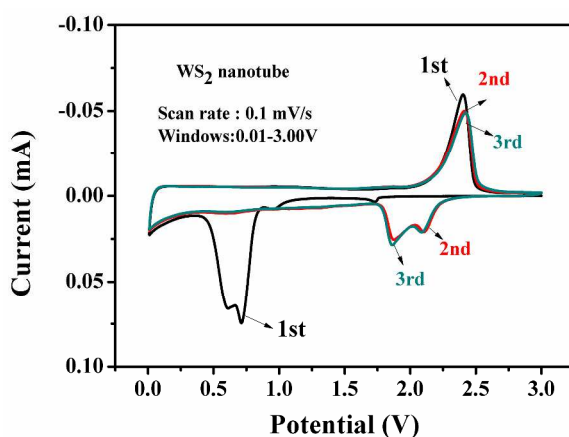


**Figure S1. Cyclic voltammetry of the  $\text{WS}_2$ -NTs anode over a voltage range of 0.01–3.00 V at a scanning rate of 0.1 mV/s;**

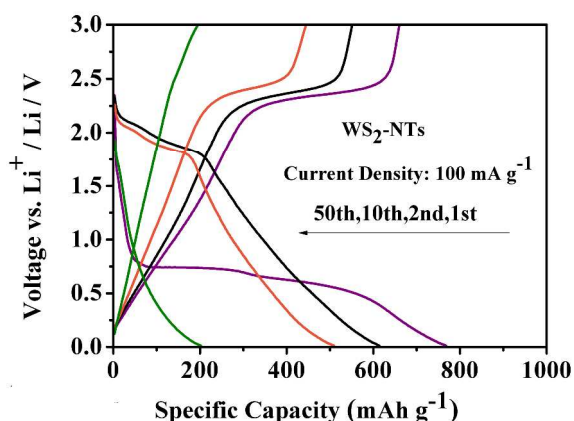


**Figure S2. Discharge/charge voltage profiles of  $\text{WS}_2$ -NTs anode at a current density of 100 mA/g;**

## References

1. Hummers, W. S.; Offeman, R. E. *J. Am. Chem. Soc.* **1958**, *80*, 1339–1339.
2. Bi, H.; Yin, K.; Xie, X.; Zhou, Y.; Wan, N.; Xu, F.; Banhart, F.; Sun, L.; Ruoff, R. S. *Adv. Mater.* **2012**, *24*, 5124–5129.